Preprints of the 21st IFAC World Congress (Virtual)
Berlin, Germany, July 12-17, 2020

# Optimal Cyclic Spooling Control for Kite-Based Energy Systems ⋆

**Joshua Daniels** * **James Reed** * **Mitchell Cobb** *
**Ayaz Siddiqui** * **Chris Vermillion** *

* *Mechanical and Aerospace Eng. Department, North Carolina State University, Raleigh, NC 27603 USA (e-mails: jldanie5@ncsu.edu, jcreed2@ncsu.edu, mcobb@ncsu.edu, asiddiq2@ncsu.edu, cvermil@ncsu.edu).*

**Abstract:** This paper presents a control strategy for optimizing the the spooling speeds of tethered energy harvesting systems that generate energy through cyclic spooling motions which consist of high-tension spool-out and low-tension spool-in. Specifically, we fuse continuous-time optimal control tools, including Pontryagin's Maximum Principle, with an iteration domain co-state correction, to develop an optimal spooling controller for energy extraction. In this work, we focus our simulation results specifically on an ocean kite system where the goal is to optimize the spooling profile while remaining at a consistent operating depth and corresponding average tether length. This paper demonstrates a 14-45% improvement (depending on the operating tether length and environmental flow speed) in power generation compared to a baseline, heuristic, control strategy.

*Keywords:* Optimal operation and control of power systems; Control of renewable energy resources; Modeling and simulation of power systems

## 1. INTRODUCTION

Wind, ocean currents, and tidal resources all represent promising and growing sources of renewable energy worldwide. On the other hand, the strongest sources of these renewable energy resources often exist in locations that are difficult to reach with conventional devices. For example, winds at 500-1000 meter altitudes routinely possess power densities exceeding 500 $W/m^2$ (Archer and Caldeira, 2008) throughout the world; however, these altitudes are unreachable with towered systems. Additionally, western boundary currents within the ocean contain a tremendous untapped resource, estimated at 25 GW (Duerr and Dhanak, 2012) in the Florida Straits and even more off of Cape Hatteras (Bane et al., 2017). However, this resource lies in waters that are hundreds of meters deep or more.

The concept of *tethered* energy systems has emerged out of the desire to harvest high-altitude winds and deep-water marine hydrokinetic (MHK) resources. In particular, by replacing conventional towers with tethers and a lifting body (a rigid wing or kite), it becomes possible to reach high-altitude winds and harvest MHK resources in deep waters. In addition to providing access to the aforementioned high power-density resources, tethered systems that deploy high lift/drag lifting bodies, often referred to as *kites* (even though the lifting body is most often a rigid wing) can perform power-augmenting *crosswind* (in the air) and *cross-current* (in the ocean) motion (Loyd, 1980). Here, the kite is flown in either figure-8 or elliptical patterns perpendicular to the prevailing flow, which has been shown to enable more than an order of magnitude more power generation than an equivalently-sized stationary system (Loyd, 1980). This potential for substantial power augmentation has led dozens of companies and research organizations, including Windlift, LLC (2019), Makani Power (2019), Ampyx Power (2019), and Minesto, Ltd. (2019) all to develop tethered systems that execute power-augmenting crosswind and cross-current motions.

Tethered systems can harvest energy in either of two ways:

- *Turbine-based generation*, sometimes referred to as "fly-gen" operation, where turbines are fixed to the kite, and power is transmitted via a conductive cable to a base station, or
- *Tension-based generation*, sometimes referred to as "ground-gen" operation, where the power is produced by a winch/generator at a base station by spooling the tether out under high tension and in under low tension.

The present work focuses on the second mode of operation. Generally speaking, the spool-out/spool-in profile utilized in this mode of operation can fall into one of two categories, or a combination thereof:

- *Multi-cycle spooling*, where the kite is spooled out under high tension continuously for multiple cycles of the path to a maximum allowable tether length, then spooled in under low tension. The low tension can be achieved by either gliding radially towards the base-station, or maintaining its path following configuration, but still flying at a low angle of attack.
- *Intra-cycle spooling*, where within a single lap, there exists a high-tension portion of that lap where the

⋆ This research was supported by the North Carolina Coastal Studies Institute's Renewable Ocean Energy Program.

kite is spooled out at a high angle of attack and a low-tension portion where it is spooled in at a low angle of attack.

In the tethered wind energy community, multi-cycle spooling has been experimentally implemented by (Williams et al., 2007), (Wood et al., 2017), (Van der Vlugt et al., 2013), and (Canale et al., 2009), whereas intra-cycle spooling has been implemented in (Houska and Diehl, 2007), and (Licitra et al., 2016). In the MHK community, (Olinger and Wang, 2015) and (Paiva and Fontes, 2017) have simulated MHK kites performing multi-cycle spooling. While a "pure" multi-cycle spooling approach that does not employ any form of intra-cycle spooling (i.e., an approach where tether is spooled out during the entirety of each figure-8 or ellipse, then spooled in under non-crosswind/non-cross-current flight) is theoretically the most efficient mechanism for power generation under a constant flow profile, several complications arise that often motivate or necessitate some level of intra-cycle spooling:

(1) Heavier-than-air tethered wind energy systems must fight gravity and often need to put energy back into the system in the corners of the figure-8 or elliptical flight paths.
(2) In significant shear environments, which are seen in both wind and MHK applications, it is desirable to maintain a relatively consistent altitude/depth, which requires a consistent tether length for a given elevation angle. Intra-cycle spooling can allow for a relatively consistent tether length and the targeting of these specific altitudes/depths.
(3) Transitioning into and out of crosswind/cross-current flight is non-trivial and must occur hundreds of times a day under the most efficient multi-cycle spooling strategy. An intra-cycle spooling strategy allows the kite to remain in crosswind/cross-current flight, using the corners of the flight path (which are naturally inclined toward delivering significantly lower tether tensions) to achieve low-tension spool-in.

For an intra-cycle spooling strategy, the spooling speed profile over the course of the figure-8 or elliptical path becomes an important decision variable for maximizing net power output. Loyd's seminal work in (1980) identifies the optimal spool-out speed as one third of the flow speed, but this is based on a simplified 2D quasi-static analysis under a direct-downwind configuration. Although significant recent research has focused on optimal tether length and elevation angle regions in (Fagiano et al., 2012), optimal holding patterns in (Licitra et al., 2016), and optimal periodic flight paths in (Houska and Diehl, 2007), (Cobb et al., 2018), (Cobb et al., 2019a), and (Cobb et al., 2019b), there is (to the best of the authors' knowledge) no result to-date that computes the optimal intra-cycle spooling profile on a 3D crosswind/cross-current flight path.

In this paper, we utilize continuous-time optimal control tools, including Pontryagin's Maximum Principle, to derive the optimal spooling profile for a tethered energy system undergoing intra-cycle spooling. For the present work, we impose a constraint that zero net spooling occurs over each lap; however, the formulation can be extended to multiple laps. Application of Pontryagin's Maximum Principle to the intra-cycle spooling problem yields optimal spooling speed profiles during the spool-in and spool-out modes of operation. Additionally, the solution of the optimal control problem provides a mechanism for selecting which parts of the path should be used for spool-in vs. spool-out operation. However, this selection mechanism is based on a co-state value that is identified to be equal to a constant but is otherwise undetermined by the optimal control conditions. In order to identify the correct value of this constant, which is necessary to ensure that the zero net spooling constraint is satisfied, the optimal spooling controller is augmented with an iteration-domain feedback controller that adjusts the estimated co-state value based on net spooling over each lap. Using a medium-fidelity model of an MHK kite system, we demonstrate the efficacy of the optimal spooling controller for multiple flow speeds, demonstrating between 14 and 45% improvement in energy production over a baseline spooling strategy.

## 2. PLANT MODEL

In this work, we focus on an ocean kite that executes figure-8 cross-current paths perpendicular to the flow direction. The overall concept of operations and coordinate systems for the kite are shown in Fig. 1. The model used for simulations and as a basis for the simplified formulation used to set up the continuous-time optimal spooling problem is adopted from our earlier work in Reed et al. (2019). We include a full summary of this model here for completeness.

### *2.1 Cross-Current Kite Dynamics*

The kite is modeled as a combination of two elements:

(1) A rigid lifting body whose forces and moments are calculated from lift, drag, buoyancy, and gravity;
(2) A tether model whose links are comprised of non-compressive damper elements, with hydrodynamic, gravitational, and buoyant forces applied at the nodes (including the end nodes), as described in detail in (Vermillion et al., 2014).

*6-DoF Lifting Body (Kite) Model* Two coordinate systems, a body-fixed and ground-fixed frame, are used to characterize the kite's dynamics. The body-fixed coordinate frame, whose origin lies at the kite's center of mass (point $k$ in Fig. 1), is characterized by orthonormal unit vectors $\boldsymbol{x}_k$, $\boldsymbol{y}_k$, and $\boldsymbol{z}_k$. The ground-fixed frame, whose origin lies at point $G$ of Fig. 1, is characterized by orthonormal unit vectors $\boldsymbol{x}_G$, $\boldsymbol{y}_G$, and $\boldsymbol{z}_G$. The state variables describing the position and orientation (and rates of change of the position and orientation) of the kite evolve according to standard nonlinear equations of motion:

$$\begin{aligned} \dot{\boldsymbol{\mu}} &= f(\boldsymbol{\mu}, \boldsymbol{\omega}) \\ \mathrm{J}\dot{\boldsymbol{\omega}} &= \boldsymbol{M}_{Net} - \boldsymbol{\omega} \times \mathrm{J}\boldsymbol{\omega} \\ \dot{\boldsymbol{x}} &= \mathrm{R}(\boldsymbol{\mu})\boldsymbol{v} \\ \mathrm{M}\dot{\boldsymbol{v}} &= (\boldsymbol{F}_{Net}(t) - \mathrm{M}\boldsymbol{\omega} \times \boldsymbol{v}) \end{aligned} \tag{1}$$

Here, the orientation of the kite is described by the vector of conventional Tait-Bryan Euler angles, $\boldsymbol{\mu} \triangleq [\ \phi \quad \theta \quad \psi\ ]^T$, where $\phi$ is roll, $\theta$ is pitch, and $\psi$ is yaw. The matrix $\mathrm{J} \in \mathbb{R}^{3\times3}$ is the apparent inertia matrix, and

$\boldsymbol{M}_{Net}$ is the sum of all applied moments, expressed in the body frame. Here, the position vector, $\boldsymbol{x} \in \mathbb{R}^3$, is the vector from the point $G$ to the point $k$, expressed in the ground frame. The vector $\boldsymbol{v}$ is the associated velocity, expressed in the body frame. The matrix $\mathrm{R} \in \mathbb{R}^{3\times3}$ is the rotation matrix from the body to the ground frame. The variable $\mathrm{M} \in \mathbb{R}^{3\times3}$ is the diagonal apparent mass matrix, $\boldsymbol{F}_{Net}$ is the sum of all forces applied to the kite expressed in the body frame, and $\boldsymbol{\omega} \triangleq [\ \omega_x \quad \omega_y \quad \omega_z\ ]^T$ is the kite's body-frame angular velocity. Finally, the function $\boldsymbol{f}(\boldsymbol{\mu}, \boldsymbol{\omega})$ is given by:

$$\boldsymbol{f}(\boldsymbol{\mu},\boldsymbol{\omega})=\begin{bmatrix} \omega_x + \omega_y \sin(\phi)\tan(\theta) + \omega_z \cos(\phi)\tan(\theta) \\ \omega_x \cos(\phi) - \omega_z \sin(\phi) \\ \left(\omega_y \sin(\phi) + \omega_z \cos(\phi)\right)\sec(\theta) \end{bmatrix}. \quad (2)$$

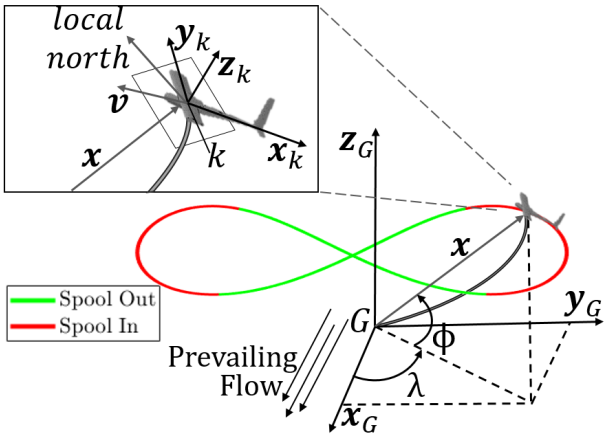


Fig. 1. Ground Station and kite coordinate systems, along with and example of an intra-cycle spooling strategy and spherical coordinate angles $\lambda$ and $\phi$.

The kite is subject to forces and moments resulting from five fluid dynamic surfaces (a fuselage, port wing, starboard wing, horizontal stabilizer and vertical stabilizer), buoyancy, gravity, and the tether. These forces and moments are calculated as:

$$\begin{aligned}\boldsymbol{F}_{Net} =& \boldsymbol{F}_{Thr} + (V\rho - m)\, g\boldsymbol{z}_G \\ &+ \frac{1}{2}\rho A_r \sum_{i=1}^{5} \|\boldsymbol{v}_{a_i}\|^2 \left(C_{L,i}\boldsymbol{u}_{L,i} + C_{D,i}\boldsymbol{u}_{D,i}\right)\end{aligned} \quad (3)$$

$$\boldsymbol{M}_{Net} = \frac{1}{2}\rho A_r \sum_{i=1}^{5} \|\boldsymbol{v}_{a_i}\|^2 \boldsymbol{r}_{a_i} \times \left(C_{L,i}\boldsymbol{u}_{L,i} + C_{D,i}\boldsymbol{u}_{D,i}\right). \quad (4)$$

Where in (3), the first term is the force exerted at the center of mass by the tether on the lifting body, the second term describes the net buoyant force, and the last term describes the fluid dynamic forces. Here, $V$ is the volume of the kite, $\rho$ is the fluid density, $m$ is the mass of the system, and $g$ is the acceleration due to gravity.

The index, $i$, refers to each of the five independent fluid dynamic surfaces. Therefore, the resulting force depends on the apparent flow at the aerodynamic center of each surface, which is calculated as:

$$\boldsymbol{v}_{a_i} = \boldsymbol{v}_f - \left(\boldsymbol{v} + \omega \times \boldsymbol{r}_{a_i}\right), \quad (5)$$

where $\boldsymbol{v}_f$ is the constant flow velocity for the simulation and $\boldsymbol{r}_{a_i}$ is the vector from the center of mass of the kite to the fluid dynamic center of the $i^{\text{th}}$ surface. The fluid dynamic coefficients of equations (3) and (4) are obtained by modeling each fluid dynamic surface independently in the Athena Vortex Lattice (AVL) software (Drela and Youngren, 2017) and parameterized as functions of the associated control surface deflections, $\delta_i$, as:

$$\begin{aligned}C_{(L,D),i}(\boldsymbol{v}_{a_i}) = C_{(L_0,D_0),i}(\boldsymbol{v}_{a_i}) + C_{(L_1,D_1),i}\delta_i \\ + C_{(L_2,D_2),i}\delta_i^2\end{aligned} \quad (6)$$

where the control sensitivity coefficients, $C_{L_1,i}$, $C_{L_2,i}$, $C_{D_1,i}$, and $C_{D_2,i}$ are obtained from AVL. The span-wise lift coefficient distributions, $C_{l,i}(y)$, obtained from the software are heuristically corrected to account for nonlinear stall behavior that is not present in AVL. This correction is given by:

$$C_{L_0,i} = \sum_{j=1}^{N_c} \begin{cases} C_{l,i}(y_{j,i}) & C_{l,i}(y_{j,i}) < C_{l_{max}}(y_{j,i}) \\ 2C_{l_{max},i}(y_{j,i}) - C_{l,i}(y_{j,i}) & C_{l,i}(y_{j,i}) \geq C_{l_{max}}(y_{j,i}) \end{cases} \quad (7)$$

where $N_c$ is the number of control points used in the AVL analysis, $y_{j,i}$ is the span-wise location of the $j^{\text{th}}$ control point of surface $i$, and $C_{l_{max}}(y_{j,i})$ is the maximum airfoil lift coefficient at the $j^{\text{th}}$ control point of surface $i$.

Finally, the unit vectors describing the direction of the lift and drag forces ($\boldsymbol{u}_{D,i}$ and $\boldsymbol{u}_{L,i}$, respectively) are calculated from the apparent wind direction vector at the $i^{\text{th}}$ aerodynamic center.

*Tether Model* The tether is modeled as a non-compressive spring damper subjected to buoyancy, gravity, and fluid drag. The expression for the net force at the end of the tether attached to the kite is given by:

$$\begin{aligned}\boldsymbol{F}_{Thr} =& \frac{1}{2}\Big( \left(\rho - \rho_T\right)\pi r_T^2 l_T g \boldsymbol{z}_G \\ &+ \frac{1}{2}\rho \|\boldsymbol{v}_{a,T}\|^2 A_{p,T} C_{D,T} \frac{\boldsymbol{v}_{a,T}}{\|\boldsymbol{v}_{a,T}\|} + \boldsymbol{F}_{Ten}\Big)\end{aligned} \quad (8)$$

where $\rho_T$ is the density of the tether, $r_T$ is the radius of the tether, $l_T$ is the un-spooled tether length, $A_{p,T}$ is the area of the tether projected in the direction of the apparent flow, $C_{D,T}$ is the drag coefficient of the tether, and $\boldsymbol{v}_{a,T}$ is the apparent flow speed at the midpoint of the tether, which is given by $\boldsymbol{v}_{a,T} = \boldsymbol{v}_f - \boldsymbol{v}/2$. Lastly, $\boldsymbol{F}_{Ten}$ is the nonlinear spring damper force which is calculated according to:

$$\boldsymbol{F}_{Ten} = \begin{cases} \boldsymbol{0} & \|\boldsymbol{x}\| < l_T, \\ \frac{1}{2}\Big( -E_y \frac{\pi r_T^2}{l_T}\left(\|\boldsymbol{x}\| - l_T\right) & \\ \quad -2\zeta\sqrt{E_y \frac{\pi r_T^2}{l_T} m}\frac{d}{dt}\|\boldsymbol{x}\|\Big)\frac{\boldsymbol{x}}{\|\boldsymbol{x}\|} & \text{otherwise,} \end{cases} \quad (9)$$

where $E_y$ is the Young's modulus of the tether and $\zeta$ is the non-dimensional damping ratio.

Un-spooled tether length, $l_T$, is calculated through the simple integration of the tether spooling speed, $\tilde{u}_T$:

$$l_T(t) = \int_0^t \tilde{u}_T(\tau)d\tau \quad (10)$$

The winch dynamics, which relate the commanded spooling speed, $u_T$, to the actual spooling speed, $\tilde{u}_T$, are based on simple first-order dynamics with upper and lower saturation limits.

## 3. CONTROL FORMULATION

The goals of the optimal intra-cycle spooling controller are twofold:

(1) Maximize average net power production over the course of a lap.
(2) Begin and end each lap at a desired tether length.

The resulting spooling profile consists of spooling speed as a function of path position. A lower-level path-following controller executes this spooling profile while also articulating control surfaces to negotiate the prescribed cross-current flight path. Fig. 2 shows how the various elements of the control system interact.

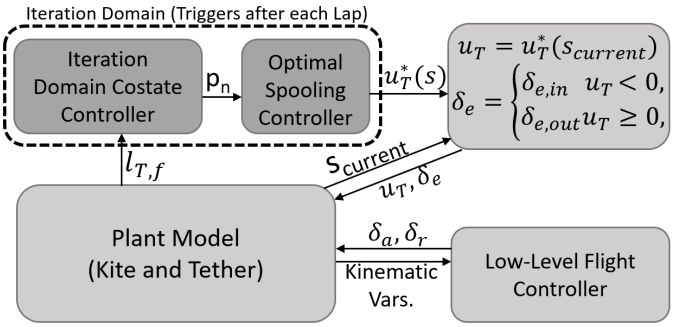


Fig. 2. Overview of entire control formulation including high level optimal spooling control and low level flight control.

### 3.1 Optimal Control Problem Formulation

In this work, we treat mechanical energy output as the control goal (with the inclusion of motor and generator efficiency maps as a topic for follow-on simulation studies). Consequently, the control goal over one lap, for a given initial time, $t_0$, and final time, $t_f$, is to maximize net mechanical energy output (the integration of tension with spooling speed), subject to the spooling dynamics of equation (10). This can be written as follows:

$$\begin{aligned}\text{Maximize} \quad & J(\tilde{u}_T) = \int_{t_0}^{t_f} T\big(\boldsymbol{\mu}(t), \boldsymbol{\omega}(t), \boldsymbol{x}(t), \boldsymbol{v}(t)\big)\tilde{u}_T(t)\, dt \\ \text{subject to} \quad & \dot{l}_T(t) = \tilde{u}_T(t), \\ & \text{Eqn. set (1)},\end{aligned}$$

where $T(\boldsymbol{\mu}(t), \boldsymbol{\omega}(t), \boldsymbol{x}(t), \boldsymbol{v}(t))$ is the tension in the tether at the ground station. The tether tension over the course of a lap depends nonlinearly on the kite's velocity and orientation, along with the characteristics of the tether. However, for a particular flow speed, flight path, and lower-level flight controller (which is assumed to be fixed for the purpose of the optimal spooling controller design), we can reasonably approximate tension as a function of spooling speed, $\tilde{u}_T$, and position along the path, $s$, which have the largest impacts. To simplify matters further, because the winch time constants (on the order of one tenth of a second) are far faster than the kite's time constants (which in an ocean environment are tens of seconds), the actual spooling speed, $\tilde{u}_T$, is approximated to be equal to the commanded winch speed, $u_T$. These assumptions lead to the following simplified optimal control problem:

$$\begin{aligned}\text{Maximize} \quad & J(u_T) = \int_{t_0}^{t_f} T\big(s(t), u_T(t)\big)u_T(t)\, dt \\ \text{subject to} \quad & \dot{l}_T(t) = u_T(t),\end{aligned}$$

where $s(t)$ is the path variable, which goes from 0 to 1 as the kite traverses the path, resetting upon each completed lap, $u_T(t)$ is the commanded spooling speed, $T\big(s(t), u_T(t)\big)$ is the tension as a function of path variable and spooling speed, and $\dot{l}_T$ is the time derivative of the tether length, which is the only state variable (not present in the objective function).

*Tension Function Characterization* Based on the simplified optimal control formulation of (11), characterizing $T(s, u_T)$ is critical. Fig. 3 represents one such tension profile (the significance of the vertical planes is described in the following sub-section); we detail the process by which we generate this profile in this sub-section. Along the path variable, $s$, axis, the surface follows a cyclic pattern. This is because the velocity of the kite increases along the straightaways in the figure-8, generating high lift and high tension, while the curves have the opposite effect. Along the spooling speed, $u_T$, direction, the surface decreases as spooling speed increases. This is due to a higher spooling speed inducing motion in the direction of flow, reducing apparent velocity, lift, and tension. The discontinuity seen at a spooling speed of zero is due to the intentional differences in angle of attack (dictated by elevator deflection) in spool-out vs. spool-in operation. When spooling speed is positive or zero, the elevator is set to maximize lift and tension, when spooling in, the elevator is deflected to reduce the angle of attack and lower tension.

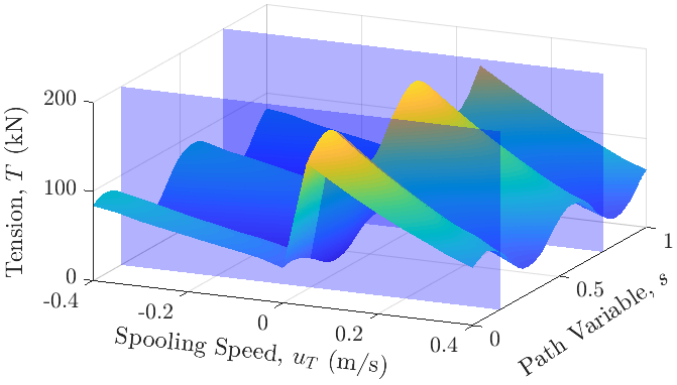


Fig. 3. Tether tension as a function of path variable and spooling speed for a figure-8 path, a flow speed of 1 m/s, and a $l_{T,des}$ of 125 m

Representative $T(s, u_T)$ functions as shown in Fig. 3 were computed at a variety of flow speeds by simulating the full system dynamics with varied spooling speed magnitude. To minimize the effect that variations in tether length have on the tension, the tether was spooled no more than 15 meters away from $l_{T,des}$. The simulations were run for 3000 seconds, and values of tension, spooling speed, and path variable were recorded. Values within 5 seconds of a transition between spooling out and spooling in were discarded to allow for transients to settle. The average

tension for values at a single spooling speed and path variable were saved into the $T(s, u_T)$ surface.

### *3.2 PMP-Based Optimal Controller*

*Optimal Spooling Control Law* In order to find the necessary conditions for a solution to the optimal control problem, the Hamiltonian, $\mathcal{H}(u_T(t), s(t), p_n)$, can be generated from the objective function and constraint. A derivation for the Hamiltonian can be found in (Kirk, 2012). The Hamiltonian for this problem is given by:

$$\mathcal{H}(u_T(t), s(t), p_n) = \big[T\big(s(t), u_T(t)\big) - p_n\big]\, u_T(t), \quad (11)$$

where $u_T(t)$ is the spooling speed, and $p_n$ is the co-state. We will soon show that the co-state for this particular problem can be interpreted as a critical tension, which is used to determine when to switch between spool-out and spool-in motions.

The conditions for optimality, also derived in (Kirk, 2012), are then given by:

(1) $\dot{l}_T = u_T(t)$, which simply represents the state dynamics of (11),
(2) $\dot{p} = 0$, indicating the co-state will be constant, and
(3) $\mathcal{H}(u_T^*(t), s(t), p^*) \geq \mathcal{H}(u_T(t), s(t), p^*)$ for all admissible $u_T(t)$, where $u_T^*(t)$ is the optimal control trajectory and $p^*$ is the optimal co-state value, which is a direct application of Pontryagin's Maximum Principle (PMP) for this problem.

Applying PMP to the Hamiltonian in (11) results in the immediate conclusions that (i) the co-state, $p_n$, has units of tension, and (ii) the optimal decision on whether to spool in ($u_T(t) < 0$) or spool out ($u_T(t) > 0$) is based on comparing $T\big(s(t), u_T(t)\big)$ with $p_n$. Thus, the co-state is referred to as a *critical tension*.

Ultimately, the optimal spooling speed at any point within the cross-current path, $u_T^*(s(t))$, given by:

$$u_T^*(s(t)) = \arg\max_{u_T}\ \mathcal{H}(u_T(t), s(t), p_n), \quad (12)$$

is visualized at two instances in the flight path, denoted by the vertical planes in Fig. 3, based on the illustrations in Figs. 4 and 5. The process for computing $u_T^*$ involves finding the spooling speed (in or out) that maximizes the area of the indicated rectangle in Figs. 4 and 5, which is equal to $\mathcal{H}(u_T(t), s(t), p_n)$. Figs. 4 and 5 show the rectangle generated from both the best spool-in speed and the best spool-out speed for reference, but only the spooling speed that produces the largest rectangle (and largest value for $\mathcal{H}(u_T(t), s(t), p_n)$) is chosen as the optimal for that value of $s$.

*Iteration-Domain Co-State Adjustment* In order to implement the control law given in equation (12), it is necessary to know the optimal value of the co-state. Because of the second condition for optimality in section 3.1, $\dot{p} = 0$, we know that the co-state is constant over a given lap. However, the optimality conditions do not provide a mechanism for computing the actual value of $p^*$. In order to find the value of the co-state which results in net-zero spooling, we implement an iteration-domain (where one iteration corresponds to a lap) proportional plus integral (PI) update law for the co-state, as follows:

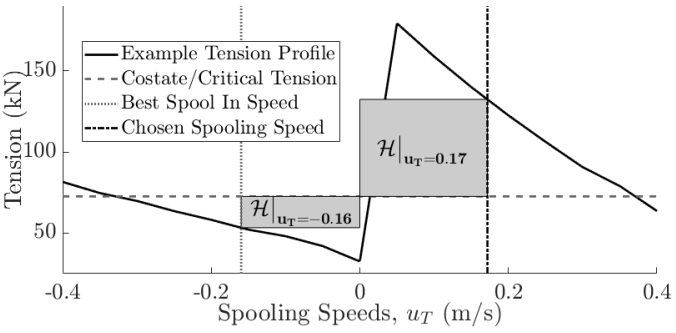


Fig. 4. Visualization of the control law with an example tension profile at a *single* value of path variable where the optimal spooling action is a *spool-out* motion at approximately 0.17 m/s.

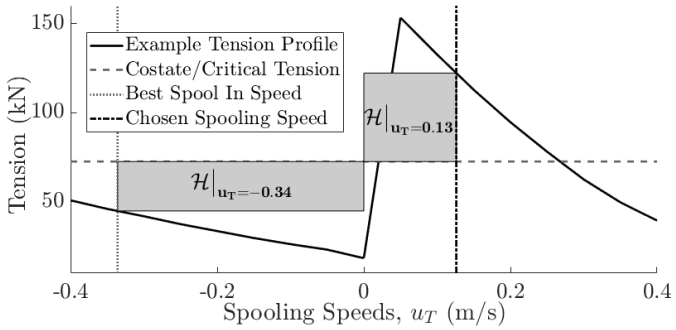


Fig. 5. Visualization of the control law with an example tension profile at a *single* value of path variable where the optimal spooling action is a *spool-in* motion at approximately 0.34 m/s.

$$p_{n+1} = k_p\big(l_{T,n} - l_{T,des}\big) + k_i \sum_{j=1}^{n} \big(l_{T,j} - l_{T,des}\big) + p_0. \quad (13)$$

In this equation, $k_p$ and $k_i$ are the proportional and integral gains respectively, $p_0$ is an initial guess for the value of the co-state, $l_{T,n}$ and $l_{T,j}$ are the tether lengths at the end of iterations (laps) $n$ and $j$ respectively, and $l_{T,des}$ is the desired tether length.

*Elevator Switching Control Law* Because we wish to maximize fluid-dynamic forces during spool-out and minimize them during spool-in, we use the elevator to trim the kite to a constant high angle of attack when spooling out and a constant, low angle of attack when spooling in. The elevator deflection, $\delta_e$, is calculated using the equation:

$$\delta_e(u_T) = \begin{cases} \delta_{e,in} & u_T < 0, \\ \delta_{e,out} & u_T \geq 0, \end{cases} \quad (14)$$

where $\delta_{e,in}$ was selected to minimize tension while spooling in, and $\delta_{e,out}$ was selected to maximize tension while spooling out.

### *3.3 Low Level Cross-Current Kite Flight Controller*

The flight control strategy is ultimately responsible for ensuring that the kite robustly tracks a prescribed figure-8 cross-current flight path. The path-tracking control strategy contains four levels, as shown in Fig. 6. Each

of these four levels accept feedback from the plant. The modular, hierarchical control structure summarized here leverages work from (Rapp et al., 2019) and is described in full detail in (Reed et al., 2019). The controller is partitioned into:

(1) A *path following controller* that accepts the path geometry, $\Gamma(s)$, and outputs a desired velocity angle, $\gamma_{des}$, as defined in (Fagiano et al., 2014).
(2) A *tangent roll angle controller*, which accepts a desired velocity angle and outputs a desired tangent roll angle, $\xi_{des}$, which is the angle between $\boldsymbol{y}_k$ and the plane tangent to the surface of the sphere of radius $\|\boldsymbol{x}\|$ at the kite's position (shown in Fig. 1) – this angle dictates the component of hydrodynamic lift that contributes to turning in order to follow the path.
(3) A *desired moments controller*, which accepts the tangent roll setpoint and side slip angle setpoint, and outputs a desired moment vector, $M_{des}$;
(4) A *control allocation module*, which accepts the desired moment vector and computes the required aileron and rudder deflections. The elevator deflection is prescribed as part of the spooling controller as described in section 3.2.

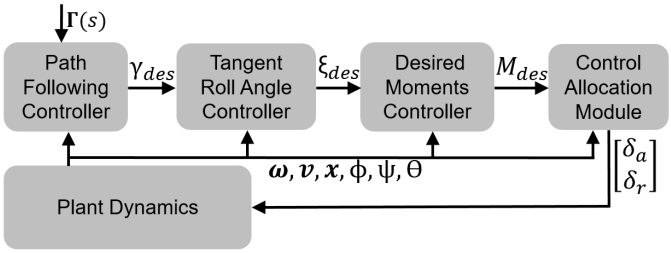


Fig. 6. The four-stage hierarchical flight controller

## 4. RESULTS

Simulations were performed over a range of flow speeds from 0.5 to 2 m/s and desired tether lengths of 125 and 200 m. All simulations had a duration of 2000 seconds and used the same path geometry, flight controller parameters, kite dimensions, and tether properties. The kite model used had a span of 10 m, reference area of 10 m$^2$, and a mass of 945 kg. Examples of the spooling strategies obtained at a target tether length 125 m and flow speed 1 m/s are shown in Figs. 7 and 8. The optimal control strategy shown in Fig. 8 was taken from the last completed figure-8 of the simulation in order to let the co-state value settle.

Another key result is the ability of the iteration domain controller to drive the tether length to the desired value by adjusting the estimated value of the co-state. In Fig. 9, a continuous plot of the tether length can be seen with the values at the start of each path highlighted. As the simulation progresses, the values of the starting locations approach the desired length.

In order to understand the power numbers, the optimally chosen spooling speeds were compared against a heuristic strategy where spooling speeds were chosen at 1/3 of the flow speed, as calculated in (Loyd, 1980). In the heuristic strategy, the kite was spooled in on the far edges of the path, for a manually chosen duration, to achieve zero net

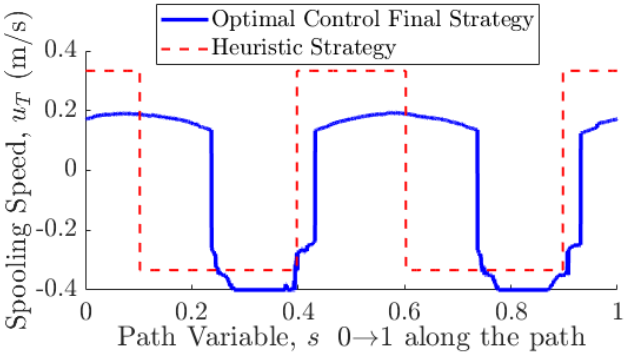


Fig. 7. Optimal and heuristically chosen spooling strategy examples over a single figure-8 lap at a flow speed of 1 m/s and a target tether length of 125 m

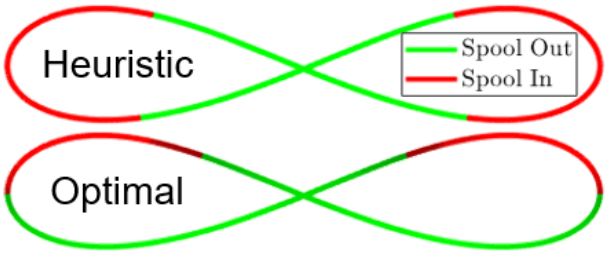


Fig. 8. Optimal and heuristically chosen spooling strategies displayed on the figure-8 path, where the brighter sections of the gradient on the optimal figure-8 correspond to the fastest spooling speed

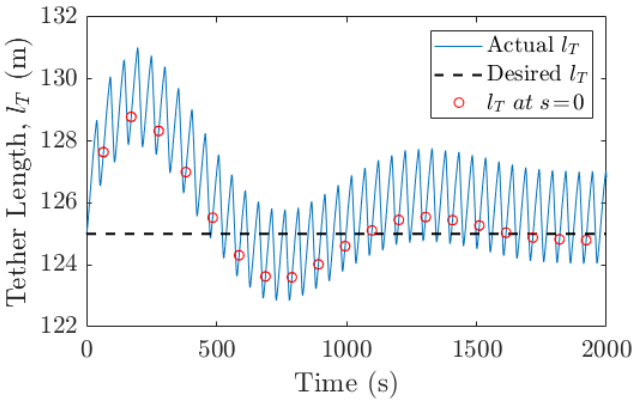


Fig. 9. Tether length over a 1 m/s flow speed simulation, demonstrating the starting/ending positions being driven to the target value

spooling. The average power was calculated after each simulation according to the equation:

$$\mathrm{P_{avg}} = \frac{\int_{t_{end}/2}^{t_{end}} T(t)\tilde{u}_T(t)dt}{t_{end} - \frac{t_{end}}{2}}. \tag{15}$$

The average power calculation was limited to the second half of each simulation to allow the value of the estimated co-state to settle. The results of the optimal control strategy and the heuristic strategy are shown in table 1.

Note that at this time, only the spooling profile, not the path geometry (which can significantly influence average

Table 1. Average power generation at various flow speeds and tether lengths.

| Flow Speed (m/s) | Desired Tether Length (m) | Average Optimal Power Gen. (kW) | Average Heuristic Power Gen. (kW) | Percent Improvement |
|---|---|---|---|---|
| 2 | 200 | 28.57 | 22.23 | 28.51% |
| 2 | 125 | 26.98 | 23.63 | 14.17% |
| 1 | 200 | 6.40 | 4.66 | 37.22% |
| 1 | 125 | 6.52 | 5.17 | 26.14% |
| 0.5 | 200 | 1.09 | 0.75 | 44.55% |
| 0.5 | 125 | 1.01 | 0.73 | 38.06% |

power generation), has been optimized. However, the same path geometry was used in all 12 simulations.

## 5. CONCLUSION

In this work, we formulated an optimal control problem that captured the essential nature of the optimal power take-off problem for an energy-harvesting kite employing cyclic spooling. We then solved that optimal control problem using continuous time optimal control techniques, resulting in an optimal spooling profile. The results demonstrated that, for a complex, nonlinear plant model, the controller is capable of augmenting power production by 14%-45% relative to a heuristic baseline strategy.

## REFERENCES

Ampyx (2019). Ampyx power website. URL `www.ampyxpower.com`.

Archer, K. and Caldeira, K. (2008). Atlas of high altitude wind power. *Carnegie Institute for Science*.

Bane, J., He, R., Muglia, M., Lowcher, C., Gong, Y., and Haines, S. (2017). Marine hydrokinetic energy from western boundary currents. *Annual Review of Marine Science*.

Canale, M., Fagiano, L., and Milanese, M. (2009). High altitude wind energy generation using controlled power kites. *IEEE Transactions on Control Systems Technology*, 18(2), 279–293.

Cobb, M., Barton, K., Fathy, H., and Vermillion, C. (2018). Iterative learning–based waypoint optimization for repetitive path planning, with application to airborne wind energy systems. *Proceedings of the IEEE Conference on Decision and Control*. Melbourne, Australia.

Cobb, M., Barton, K., Fathy, H., and Vermillion, C. (2019a). An iterative learning approach for online path optimization for tethered energy systems undergoing cyclic spooling motion. *Proceedings of the American Control Conference*. Philadelphia, PA.

Cobb, M., Barton, K., Fathy, H., and Vermillion", C. (2019b). Iterative learning-based path optimization for repetative path planning, with application to 3D crosswind flight of airborne wind energy systems. *Transactions on Control Systems Technology*.

Drela, M. and Youngren, H. (2017). AVL. URL `web.mit.edu/drela/Public/web/avl/`.

Duerr, A.E. and Dhanak, M.R. (2012). An assessment of the hydrokinetic energy resource of the Florida current. *IEEE Journal of Oceanic Engineering*, 37(2), 281–293.

Fagiano, L., Zgraggen, A.U., Morari, M., and Khammash, M. (2014). Automatic crosswind flight of tethered wings for airborne wind energy: Modeling, control design, and experimental results. *IEEE Transactions on Control Systems Technology*, 22(4), 1433–1447. doi:10.1109/TCST.2013.2279592.

Fagiano, L., Milanese, M., and Piga, D. (2012). Optimization of airborne wind energy generators. *International Journal of robust and nonlinear control*, 22(18), 2055–2083.

Houska, B. and Diehl, M. (2007). Optimal control for power generating kites. In *2007 European Control Conference (ECC)*, 3560–3567. doi:10.23919/ECC.2007.7068861.

Kirk, D.E. (2012). *Optimal control theory: an introduction*. Courier Corporation.

Licitra, G., Sieberling, S., Engelen, S., Williams, P., Ruiterkamp, R., and Diehl, M. (2016). Optimal control for minimizing power consumption during holding patterns for airborne wind energy pumping system. In *2016 European Control Conference (ECC)*, 1574–1579. IEEE.

Loyd, M. (1980). Crosswind kite power. *Journal of Energy*, 4(3), 106–111.

Makani (2019). Makani website. URL `makanipower.com`.

Minesto (2019). Minesto website. URL `www.minesto.com`.

Olinger, D.J. and Wang, Y. (2015). Hydrokinetic energy harvesting using tethered undersea kites. *Journal of Renewable and Sustainable Energy*, 7(4), 043114.

Paiva, L.T. and Fontes, F.A. (2017). Optimal control of underwater kite power systems. In *2017 International conference in energy and sustainability in small developing economies (ES2DE)*, 1–6. IEEE.

Rapp, S., Schmehl, R., Oland, E., Smidt, S., Haas, T., and Meyers, J. (2019). A modular control architecture for airborne wind energy systems. In *AIAA Scitech 2019 Forum*, 1419.

Reed, J., Daniels, J., Siddiqui, A., Cobb, M., and Vermillion, C. (2019). Optimal exploration and charging for an autonomous underwatervehicle with energy-harvesting kite. Under review.

Van der Vlugt, R., Peschel, J., and Schmehl, R. (2013). Design and experimental characterization of a pumping kite power system. In *Airborne Wind Energy*, 403–425. Springer.

Vermillion, C., Grunnagle, T., Lim, R., and Kolmanovsky, I. (2014). Model-based plant design and hierarchical control of a prototype lighter-than-air wind energy system, with experimental flight test results. *IEEE Transactions on Control Systems Technology*, 22, 531–542.

Williams, P., Lansdorp, B., and Ockels, W. (2007). Modeling and control of a kite on a variable length flexible inelastic tether. In *AIAA Modeling and Simulation Technologies Conference and Exhibit*, 6705.

Windlift (2019). Windlift website. URL `www.windlift.com`.

Wood, T., Hesse, H., and Smith, R. (2017). Predictive control of autonomous kites in tow test experiments. *IEEE Control Systems Letters*, 1, 110–115.